Nanoscale

PAPER

View Article Online
View Journal | View Issue

Cite this: *Nanoscale*, 2025, **17**, 7091

What makes β-$NaYF_4$:Er^{3+},Yb^{3+} such a successful luminescent thermometer?

Markus Suta

Luminescence thermometry has emerged as a promising approach for remote, non-invasive temperature sensing at the nanoscale. One of the simplest approaches in that regard is single-ion luminescence Boltzmann thermometry that exploits thermal coupling between two radiatively emitting levels. The working horse example for this type of luminescence thermometry is undoubtedly the green-emitting upconversion phosphor β-$NaYF_4$:Er^{3+},Yb^{3+} exploiting the thermal coupling between the two excited $^2H_{11/2}$ and $^4S_{3/2}$ levels of Er^{3+} for this purpose. Within this tutorial article, I would like to give a theoretically motivated account on the underlying reasons for the experimentally recorded success of this material for Boltzmann thermometry referring to time-resolved data on both the bulk and nanocrystalline material. Guidelines are established and both advantages and potential pitfalls in β-$NaYF_4$:Er^{3+},Yb^{3+} for luminescence thermometry are given.

Received 24th October 2024,
Accepted 20th January 2025

DOI: 10.1039/d4nr04392h

rsc.li/nanoscale

Inorganic Photoactive Materials, Institute of Inorganic Chemistry, Heinrich Heine University Düsseldorf, Universitätsstraße 1, 40225 Düsseldorf, Germany.
E-mail: markus.suta@hhu.de

Markus Suta

Markus Suta studied Chemistry (MSc) at the University of Siegen, Germany, and obtained his PhD degree in Chemistry in Claudia Wickleder's group in 2017. He followed up with a second degree in Physics (MSc) with specialization in Theoretical Physics in Thomas Mannel's group in Siegen. From 2018 to 2021, he has been working as a postdoctoral researcher in Andries Meijerink's group at Utrecht University, The Netherlands. Since 2021, he has been holding a tenure track position for Inorganic Photoactive Materials at the Heinrich Heine University Düsseldorf, Germany. His interests lie in the development and a fundamental understanding of new inorganic phosphors for various applications such as LEDs, luminescent thermometry, upconversion, as well as a better understanding of nonradiative transitions. For that purpose, he and his group combine inorganic synthesis and structural chemistry in solid-state systems with advanced optical characterization by means of luminescence spectroscopy as well as theoretical modelling.

Introduction

Remote temperature sensing by means of a luminescence signal (luminescence thermometry) has revolutionized phosphor research and has been one of its dominating areas since the early 2000s.[1–6] Among the various possibilities to use temperature-dependent luminescence for calibration in thermometry, self-referenced ratiometric thermometry is one of the simplest approaches.[4] It exploits the fact the luminescence intensity ratio (LIR) of thermally coupled, radiatively emitting excited states from the same electron configuration follows Boltzmann's law thus enabling an appealingly simple calibration of such an optical thermometer. A representative example of this concept are the green-emitting $^2H_{11/2}$ and $^4S_{3/2}$ levels of the Er^{3+} ion discussed within this work. Usually, the energy splitting between thermally coupled electronic states should be in the order of the thermal energy k_BT to be probed (k_B is Boltzmann's constant), which is roughly 10^2–10^3 cm^{-1} for temperatures around room temperature and 10^1–10^2 cm^{-1} for cryogenic temperatures. The trivalent lanthanoid ions with the intraconfigurational $4f^n$–$4f^n$ transitions (n = 2 for Pr^{3+} to n = 12 for Tm^{3+}) in the ultraviolet (UV), visible, and near infrared (NIR) range are naturally suited for that purpose because the low linewidth of the related emission lines allows to spectrally resolve such low energy gaps.[7] Thus, thermal coupling between different spin–orbit levels of the lanthanoids is useful for thermometry at around room temperature and above,[7,8] while thermal coupling between different crystal field states is required for cryogenic temperature measurements exploiting single-ion Boltzmann thermometry.[9–11] Although it is often argued in literature that the energy gap should not exceed

2000 cm^{-1} for effective thermometry, it should be noted that this statement depends on the temperature of interest, and energy gaps beyond 2000 cm^{-1} can be easily exploited if the intrinsic non-radiative coupling between excited states is sufficiently strong or temperatures are high enough.[12–14] This is usually encountered in so-called crossover luminescent thermometers that probe thermal coupling between excited states of different electronic configurations such as Pr^{3+},[15–19] selected divalent lanthanoid ions,[14,20–23] or thermally activated delayed fluorescent emitters.[24–27] In the context of this tutorial article, only the case of classic ratiometric Boltzmann luminescent thermometers will be considered.

Although the electronic structure of the trivalent lanthanoids formally offers a rich variety of possibilities for luminescent thermometry, the prominent upconversion phosphor β-$NaYF_4$:Er^{3+},Yb^{3+} stands out in this regard.[28,29] In this phosphor, NIR excitation of the Yb^{3+} ions at 980 nm leads to bright green upconverted emission from the thermally coupled excited $^2H_{11/2}$ and $^4S_{3/2}$ levels of Er^{3+}. Probably, also the excellent size and habitus control of nanocrystalline β-$NaYF_4$:Er^{3+}, Yb^{3+} without significant loss in its upconversion performance has additionally contributed to the huge recorded success of that compound in the field.[30,31]

Er^{3+} was established as one of the pioneering ratiometric luminescent thermometers with various milestones, first in fluoridic ZBLAN fibers in 1990,[32] then in $BaTiO_3$ in 2004,[33] and finally as nanocrystalline β-$NaYF_4$:Er^{3+},Yb^{3+} in 2009.[34] Since then, the latter compound has been constantly exploited as the working horse example for tests of luminescence thermometry in real-case applications including catalysis and microflow reactors,[35–39] probing of Brownian motion,[40,41] thermal imaging of microelectronic circuits,[42] plasmonic heating[43,44] and heat transfer along lipid bilayers.[45,46] Other examples include temperature monitoring within a mitochondrium,[47] pushing of the single nanothermometric level within a heated nanowire,[48] or recording of density fluctuations of water.[41] The established success of this upconversion phosphor for thermometry even allowed to shed light on potential biases in luminescence nanothermometry.[49–52] But what makes this phosphor stand out compared to many other lanthanoid-activated inorganic compounds that leads to this constantly recorded experimental success? Based on recently established theoretical guidelines for Boltzmann thermometers,[8] I would like to elaborate on the consequences for Er^{3+} and demonstrate from thermodynamic and kinetic viewpoints – using both measured and reported data – why β-$NaYF_4$:Er^{3+},Yb^{3+} is actually such a successful luminescent Boltzmann thermometer and what practical issues can potentially arise when it is used in its nanocrystalline rather than microcrystalline form.

Results and discussion

Synthesis

A microcrystalline sample of the nominal composition β-$NaY_{0.80}Er_{0.02}Yb_{0.18}F_4$ (hereafter simply referred to as β-$NaYF_4$:Er^{3+},Yb^{3+}) has been prepared by a conventional solid-state chemical route. For that purpose, Y_2O_3 (99.999%, Chempur), Er_2O_3 (99.999%, Chempur) and Yb_2O_3 (99.99%, smart-elements) were dissolved in the respective stoichiometric amounts in 6 mL concentrated HCl (37%, Fisher Scientific) upon heating at around 100 °C until the solution became completely transparent. After that, the solvent level was carefully reduced at 80 °C and gradually diluted with distilled H_2O. Subsequently, the pH was increased to 5 by dropwise addition of aqueous, concentrated NH_3 (28–30 wt%, Thermo Scientiifc) solution. Finally, an excess of saturated $(NH_4)_2CO_3$ (98%, Thermo Scientific) solution was added resulting in a precipitation of the basic rare earth carbonates. The dried colourless residue was reacted with 3 eq. NH_4HF_2 (98%, Thermo Scientific) at 120 °C for 1 h, thoroughly mixed with additional 3 eq. NH_4HF_2 and reacted at 150 °C before final reaction with 2 eq. $NaBF_4$ (98%, Chempur) at 500 °C under a N_2 atmosphere. According to X-ray powder diffraction, it was phase pure, although some reflections are shifted compared to the reflections of the database pattern of β-$NaYF_4$ (ICSD: 51916) based on the presence of the smaller Er^{3+} and Yb^{3+} ions that change the lattice constants of the prepared compound.

Characterization

The sample purity was assessed by means of X-ray powder diffraction on a X'Pert diffractometer (Malvern Panalytical, Cu K_α radiation) working with Bragg–Brentano geometry. The powdered sample was measured in reflection mode on an Al sample holder. Steady-state and time-resolved photoluminescence were measured on a FLS1000 photoluminescence spectrometer (Edinburgh Instruments) equipped with a 450 W Xe lamp, Czerny-Turner double grating monochromators (focal length 2 × 325 mm, blazed at 400 nm and 500 nm, respectively) in both the excitation and emission compartment, and a thermoelectrically (−20 °C) cooled PMT-980 detector (Hamamatsu). A continuous-wave laser with variable power density emitting at λ = 980 nm (PhotonTec, estimated power density of the unfocused beam for the experiments in this work: ~5.5 mW cm^{-2}) was used as an excitation source, while the luminescence decay of the green emission was recorded with a VPL-510 laser (Edinburgh Instruments; λ_{ex} = (515 ± 5) nm, 70 mW average incident power, variable temporal pulse width, repetition rate f = 125 Hz). Upconversion emission spectra were corrected for the grating efficiency and detector sensitivity. Temperature-dependent luminescence spectra were acquired with a Linkam Scientific THMS600 cell (accuracy ± 0.1 °C) between 77 K and 823 K.

Thermodynamic assessment

In its dynamic working range, the LIR, $R_{21}(T)$, between two emission peaks with intensities I_{20} and I_{10} for the transitions from two thermally coupled excited levels $|2\rangle$ and $|1\rangle$ to a common ground level $|0\rangle$ of a luminescent Boltzmann thermometer follows the simple calibration law

$$R_{21}(T) = \frac{I_{20}}{I_{10}} = C\frac{g_2}{g_1}\exp\left(-\frac{\Delta E_{21}}{k_B T}\right) \quad (1)$$

with C as electronic pre-factor (see below), g_2 and g_1 as the degeneracies of the excited levels, ΔE_{21} as the mutual energy gap between the two thermally coupled excited levels $|2\rangle$ and $|1\rangle$, and k_B as Boltzmann's constant.

For a better mechanistic understanding of luminescent Boltzmann thermometers, it is advisable to use microcrystalline instead of nanocrystalline samples to avoid an impact of surface-attached ligands or surrounding solvent molecules to non-radiative transitions. Typically, the two green-emitting spin–orbit levels $^2H_{11/2} = |2\rangle$ and $^4S_{3/2} = |1\rangle$ of the Er^{3+} ion are probed for luminescence Boltzmann thermometry.[14] In the host β-$NaYF_4$, they are separated by an energy gap of ΔE_{21} = (650 ± 10) cm^{-1} according to high-resolution excitation spectra of a representative microcrystalline sample at 77 K (see Fig. 1(a)), in good agreement to earlier reports.[52,53] It is noteworthy that many publications report varying values for this energy gap,[35–39,54,55] but photoluminescence excitation spectra offer an unambiguous reference for this value that can be related to the estimated gap according to a Boltzmann fit of the temperature-dependent LIR (see Fig. 1(b) and (c)). Given that value for ΔE_{21}, it can be estimated that the thermodynamic optimum operating temperature range for an Er^{3+}-based Boltzmann thermometer, in which it works with highest possible statistical precision,[8] is given by

$$T_{opt} \in \left[\frac{\Delta E_{21}}{(2+\sqrt{2})k_B}, \frac{\Delta E_{21}}{2k_B}\right] = [275\,K, 468\,K] \quad (2)$$

In that temperature range, there is a compromise between high relative sensitivity $S_r(T)$ and appreciable signal-to-noise ratio of the emission peaks stemming from both excited levels. Thus, Er^{3+} is particularly suited as a luminescent thermometer for biologically relevant temperatures, which nicely coincides with its application in upconversion phosphors for bioimaging applications.[56] In the optimum temperature range according to eqn (2), the relative sensitivities of the Er^{3+}-based Boltzmann thermometer vary between $S_r(T = 275\ K) = 1.24\%\ K^{-1}$ and $S_r(T = 468\ K) = 0.43\%\ K^{-1}$. It should be noted, however, that the relative sensitivity does not fully determine the performance of a luminescent thermometer, but rather the overall expected relative statistical uncertainty, which will be addressed below.

A second important feature relates to the radiative transition rates of both involved emission lines. Usually, the low intensity of the higher energetic emission poses a fundamental limitation to the precision of any luminescent Boltzmann thermometer as its intensity is typically dominated by the thermal population of the higher excited level and thus, the exponential Boltzmann factor of eqn (1). However, an additionally beneficial factor for the overall precision of the luminescent Boltzmann thermometer can be the pre-constant Cg_2/g_1 based on the motivation that a LIR should be in the order of 10° in a regarded temperature range for highest precision.

In the case of Er^{3+}, it is $g_2 = 12$ and $g_1 = 4$, if thermalization between the different Stark states in a ligand field is assumed (which is given in the optimum temperature range according to eqn (2)). It has been demonstrated that a thermodynamically advisable value for Cg_2/g_1 should be[8]

$$C_{opt}\frac{g_2}{g_1} = \frac{\exp(2+\sqrt{2})}{\sqrt{2}} \approx 21.5 \quad (3)$$

The electronic pre-constant C is connected to the spontaneous emission rates A_{20} and A_{10} for the radiative transitions $|2\rangle \rightarrow |0\rangle$ and $|1\rangle \rightarrow |0\rangle$,

$$C = \frac{A_{20}}{A_{10}} = \frac{\beta_{20}k_{2r}}{\beta_{10}k_{1r}} \quad (4)$$

where β_{20} and β_{10} are the branching ratios of the respective transitions and k_{2r} and k_{1r} are the (experimentally accessible) total radiative decay rates of the excited levels $|2\rangle$ and $|1\rangle$. It should be noted that no emission energies enter eqn (4), as is commonly found in literature due to the fact that most modern spectrometers measure intensities by photon counting.[8]

In the case of Er^{3+} in β-$NaYF_4$, careful diffuse reflectance measurements on microcrystalline powders allow an estimate for the exponential pre-constant for Er^{3+} of Cg_2/g_1 = 18.9, which is close to the optimum value for highest precision according to eqn (3). In contrast, Judd–Ofelt calculations rather yield a value of Cg_2/g_1 = 7.7 indicating that the range of possible C values in literature can vary significantly.[57,58] Such high values for the exponential prefactor mean that the intensity of the higher energetic $^2H_{11/2} \rightarrow {}^4I_{15/2}$-based emission of Er^{3+} at around 525 nm shows a higher spontaneous radiative emission rate or oscillator strength. This fact becomes particularly prominent at higher temperatures, at which the $^2H_{11/2} \rightarrow {}^4I_{15/2}$-based emission at around 525 nm is even more intense than the $^4S_{3/2} \rightarrow {}^4I_{15/2}$-based emission at around 540 nm (see Fig. 1(b)). Such a feature is very uncommon for most other thermometrically exploited lanthanoid ions such as Nd^{3+}, Gd^{3+}, or Eu^{3+}, for which it is generally $A_{20} \lesssim A_{10}$ and thus, $Cg_2/g_1 < 10^1$. It should be noted that photonic effects can additionally affect this pre-constant and have to be taken into account for nanothermometers in the vicinity *e.g.*, mirroring surfaces.[52] In this particular compound, an exponential pre-factor of $Cg_2/g_1 = 5.52 \pm 0.21$ is estimated, although the error range is probably even larger given that it is in principle estimated from an extrapolation of the LIR formally infinite temperatures. The overall unusually high value (partially related to the high J degeneracy of the $^2H_{11/2}$ level) electronically contributes to an appreciable signal-to-noise ratio from both green emission band and thus, enhances the overall precision of the Er^{3+}-based luminescent thermometer.

In its optimum performance range (see eqn (2)) and with an intensity of the $^4S_{3/2} \rightarrow {}^4I_{15/2}$-based emission of $I_{10} = 10^6$ cts, the minimum expected relative uncertainty σ_T/T of the Er^{3+}-related luminescent thermometer is constantly below 0.08% according to[8]

$$\frac{\sigma_T}{T} = \frac{k_B T}{\Delta E_{21}}\frac{1}{\sqrt{I_{10}}}\sqrt{1+\frac{1}{R_{21}(T)}} \quad (5)$$

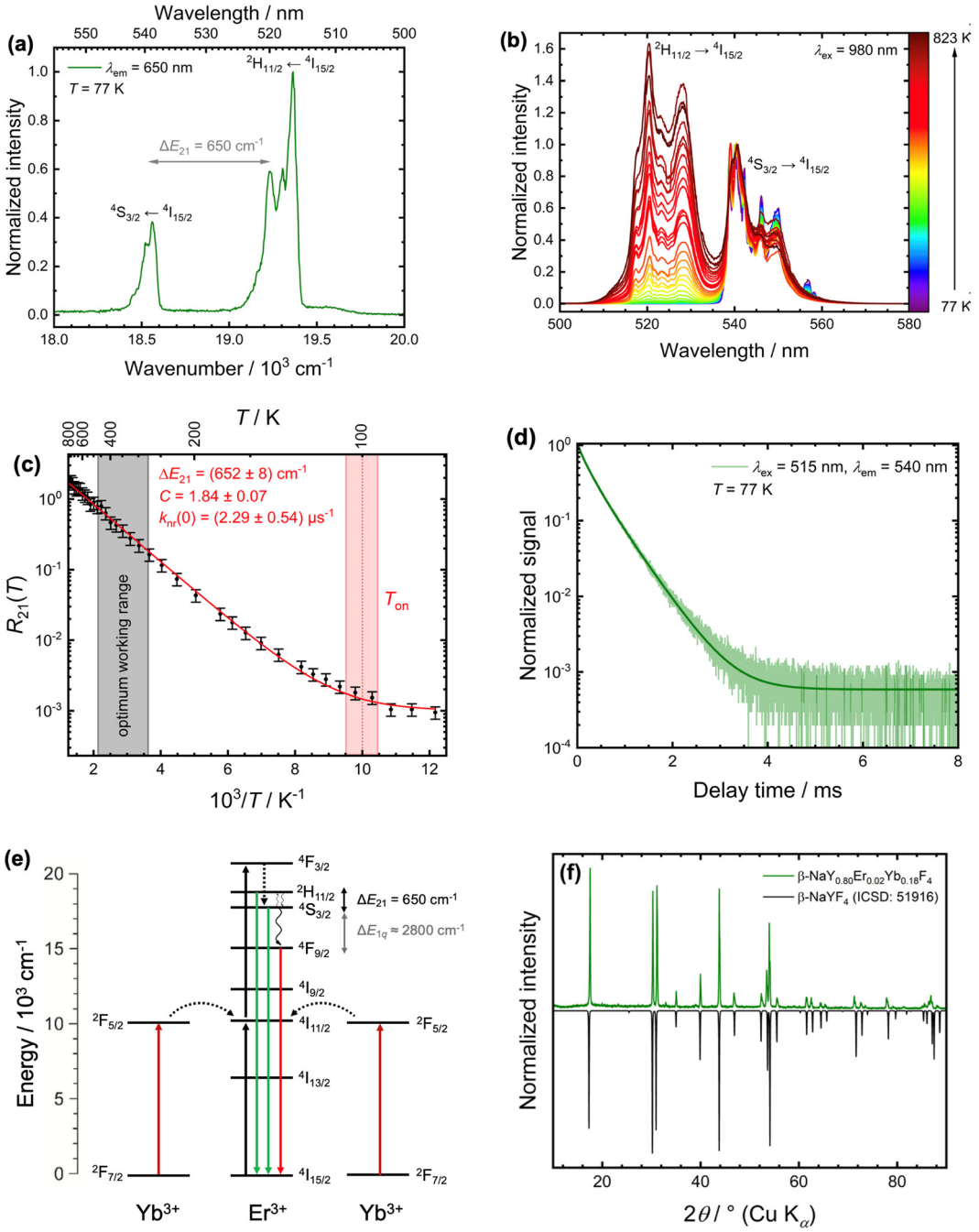

Fig. 1 Characteristics of microcrystalline β-$NaYF_4$:2 mol%Er^{3+},18 mol%Yb^{3+} for luminescence Boltzmann thermometry. (a) High-resolution photoluminescence excitation spectra at T = 77 K (plotted against wavenumbers) upon monitoring the red $^4F_{9/2} \rightarrow {}^4I_{15/2}$-based emission at λ_{em} = 650 nm. The effective energy gap between the $^4S_{3/2}$ and $^2H_{11/2}$ level is indicated. (b) Temperature-dependent upconversion spectra of β-$NaYF_4$:2 mol% Er^{3+},18 mol%Yb^{3+} upon near infrared excitation (λ_{ex} = 980 nm) between 77 K and 823 K. The spectra were normalized with respect to the emission peak at 540 nm. (c) Plot of the LIR of the two green emission bands of Er^{3+} against reciprocal temperature in the measured temperature range. Integration ranges were between 510 nm and 533 nm as well as 533 nm and 555 nm, respectively. The red line corresponds to a fit according to eqn (1) with an offset term related to $k_{nr}(0)$. Both the estimated onset temperature T_{on} and the optimum working range according to eqn (2) are indicated. (d) Luminescence decay curve of the $^4S_{3/2} \rightarrow {}^4I_{15/2}$-based emission ($\lambda_{em}$ = 540 nm, spectral bandwidth $\Delta\lambda$ = 1.5 nm) upon direct excitation into the $^2H_{11/2}$ level (λ_{ex} = 515 nm) at T = 77 K. The solid line represents an effective triexponential fit and gives an intensity-weighted average decay time of $\langle\tau\rangle$ = 0.41 ms. (e) Schematic energy level scheme for the cooperative upconversion process between Yb^{3+} and Er^{3+}. Solid, straight arrows depict absorption (upward) or emission (downward) pathways. Relevant nonradiative processes in this work are indicated by curly black arrows. (f) Powder X-ray diffraction pattern (Cu K_α radiation) of as-synthesized microcrystalline β-$NaYF_4$:2 mol%Er^{3+},18 mol%Yb^{3+} compared to a diffraction pattern derived from single-crystal structure data of β-$NaYF_4$ (ICSD: 51916).

with all symbols as defined before. For microcrystalline as well as high-quality nanocrystalline β-$NaYF_4$:Er^{3+},Yb^{3+}, these intensities are easily achievable with low incident power densities. In addition, upconverted emission is particularly background-free thus making Er^{3+} a very precise luminescent Boltzmann thermometer. Higher incident power densities of the NIR excitation light can, however, introduce additional systematic deviations based on a three-photon process that leads to interfering $^2H_{9/2} \rightarrow {}^4I_{13/2}$-based emission in the green spectral range.[59,60]

Kinetic assessment

So far, it has been demonstrated that the green-emitting $^2H_{11/2}$ and $^4S_{3/2}$ levels of Er^{3+} fulfil many of the required conditions for thermodynamically motivated optimum performance as a single-ion luminescent Boltzmann thermometer in the physiological temperature range with high statistical precision. Besides this thermodynamic motivation, the kinetic interplay between radiative decay of the lower energetic excited $^4S_{3/2}$ level and non-radiative coupling between the excited levels is relevant for the dynamic working range of any single ion as a luminescent Boltzmann thermometer.[8,61]

In the case of Er^{3+}, the radiative decay rate (corrected for reabsorption effects) of the $^4S_{3/2}$ level in β-$NaYF_4$:0.1 mol%Er^{3+} is k_{1r} = 1.55 ms^{-1}, in good agreement with earlier calculations.[57,62] This competition poses a natural, kinetically induced onset temperature T_{on} for such a luminescent Boltzmann thermometer below which the two excited states decouple and thermal equilibrium is not sustained anymore since the nonradiative absorption rate cannot compete with radiative decay of the lower energetic excited level anymore.[8,61] The nonradiative transitions among $4f^n$ spin–orbit levels is most dominantly governed by the energy gap law of multiphonon transitions.[63] It was demonstrated that the energy gap ΔE_{21} is ideally bridged by no more than p = 2 vibrational modes to ensure that the onset temperature for thermal equilibrium is below the optimum range as defined in eqn (2).[8] This is clearly given in the case of β-$NaYF_4$:Er^{3+},Yb^{3+} with a cutoff phonon energy of $\hbar\omega_{cut}$ = 450 cm^{-1} (ref. 64) and the respective energy gap of ΔE_{21} = (650 ± 10) cm^{-1}. If nonradiative thermal coupling involves p = 2 effective phonon modes of energy $\hbar\omega_{eff}$ = $\Delta E_{21}/p$, the expected onset temperature T_{on} for Boltzmann behaviour of the LIR can be derived as[8]

$$T_{on} = \frac{\hbar\omega_{eff}}{k_B \ln\left[1 + \left(\frac{g_2 k_{nr}(0)}{k_1}\right)^{1/p}\right]} \quad (6)$$

Fig. 1(c) depicts the temperature-dependent LIR of the two green emission bands of Er^{3+} in the representative microcrystalline β-$NaYF_4$:2 mol%Er^{3+}, 18 mol% Yb^{3+} sample (see Synthesis section for more details) between 77 K and 823 K obtained upon excitation with 980 nm to eliminate background for higher accuracy. From the estimated onset temperature of T_{on} = (100 ± 5) K according to the recorded LIR between the $^2H_{11/2}$- and $^4S_{3/2}$-based emission bands in the green range and an average decay rate of k_1 = 2.43 ms^{-1} (see Fig. 1(d)), an intrinsic nonradiative transition rate of $k_{nr}(0)$ = (2.29 ± 0.54) μs^{-1} governing the coupling the $^2H_{11/2}$ and $^4S_{3/2}$ level can be estimated from eqn (6). The value appears reasonable given the fact that detection of the luminescence decay trace of the $^4S_{3/2}$-based emission of Er^{3+} in β-$NaYF_4$ at 77 K (see Fig. 1(d)) upon excitation into the $^2H_{11/2}$ level does not reveal any rise component even if the pulse width is decreased to 0.1 μs and the decay is regarded in a μs time range. This implies that the feeding of the $^4S_{3/2}$ level proceeds faster than 1 μs, matching the upper estimate for $k_{nr}(0)$. Compared to many other lanthanoid ions with similar two-phonon nonradiative transitions between their excited levels such as Eu^{3+}, the intrinsic nonradiative coupling between the excited levels of Er^{3+} is unusually strong and indicates an induced electric dipolar nature of the respective nonradiative transition.[8] A measure for that can be the relevant matrix elements for induced electric dipolar transitions as originally suggested by Judd and Ofelt.[65,66] For the $^2H_{11/2} \leftrightarrow {}^4S_{3/2}$ transition, they read $\|\langle U^{(k)}\|\rangle^2$ ($\|\langle U^{(2)}\|\rangle^2$ = 0.000, $\|\langle U^{(4)}\|\rangle^2$ = 0.2002, $\|\langle U^{(6)}\|\rangle^2$ = 0.0097) according to Carnall *et al.*,[53] which are higher than for most other thermometrically relevant nonradiative transitions within the trivalent lanthanoids. For comparison, a respective two-phonon non-radiative transition rate between the $^5D_1$ and $^5D_0$ levels of Eu^{3+} in *e.g.*, $LaPO_4$ or $LaBO_3$ is in the order of only 10^1 ms^{-1} and indicates a magnetic dipolar transition,[67] as was also originally proposed by Weber.[68]

According to the energy gap law, it could be questioned why no host compound with higher cutoff phonon energies resonant to the energy gap ΔE_{21} such as aluminates, vanadates, phosphates, or borates could be more recommendable for Er^{3+} as a luminescent Boltzmann thermometer. The reason for that point lies in the special electronic landscape of the Er^{3+} ion. Besides the two thermally coupled green emitting levels, there is also a red-emitting lower energetic $^4F_{9/2}$ level *ca.* 2800 cm^{-1} below the $^4S_{3/2}$ level (see Fig. 1(e)). Thus, even if a higher cutoff phonon energy may accelerate the nonradiative thermal coupling between the green-emitting $^2H_{11/2}$ and $^4S_{3/2}$ levels of Er^{3+}, competitive nonradiative multiphonon relaxation from the $^4S_{3/2}$ level to the $^4F_{9/2}$ level also becomes more effective thus increasing the total decay rate k_1 of the $^4S_{3/2}$ level that the nonradiative absorption rate to the $^2H_{11/2}$ level has to compete with. An example demonstrating this problem is YVO_4:0.1 mol%Er^{3+}. This compound has a higher cutoff phonon energy of $\hbar\omega_{cut}$ = 890 cm^{-1} resulting in a higher decay rate of k_1 = 10^2 ms^{-1} of the $^4S_{3/2}$ level in that host due to faster non-radiative relaxation to the lower energetic $^4F_{9/2}$ level.[69] In contrast, no phonon modes with an energy of 650 cm^{-1} are present in xenotime-type YVO_4 excluding a resonant one-phonon process for the non-radiative coupling between the $^2H_{11/2}$ and $^4S_{3/2}$ level of Er^{3+} in that host.[70,71] Consequently, the onset temperature for thermalization between those two green-emitting levels in YVO_4:0.1 mol%Er^{3+} is only at T_{on} = 135 K,[69] even above the respective value in β-$NaYF_4$:Er^{3+}(Yb^{3+}). The non-radiative coupling strength between the $^2H_{11/2}$ and $^4S_{3/2}$ level can be estimated by $k_{nr}(0) \approx 7$ μs^{-1} in

YVO_4:0.1 mol%Er^{3+} based on the reported spectroscopic data, in the same order of magnitude as for β-$NaYF_4$:Er^{3+},Yb^{3+}.

Thus, at high temperatures, nonradiative multiphonon relaxation from the $^4S_{3/2} = |1\rangle$ to the red-emitting $^4F_{9/2} = |q\rangle$ level can become a general limitation for β-$NaYF_4$:Er^{3+},Yb^{3+} as a luminescent Boltzmann thermometer. However, given a mutual energy gap of $\Delta E_{1q} \approx 2800$ cm^{-1}, it can be derived from the thermal occupation of phonons that the onset temperature for stimulated (and thus, thermally accelerated) nonradiative relaxation from the $^4S_{3/2}$ to the red-emitting $^4F_{9/2}$ level is about[8]

$$T_q = 0.2227 \frac{\Delta E_{1q}}{k_B} \approx 900\,K \quad (7)$$

This makes Er^{3+} formally suited as a classic Boltzmann thermometer over a wide temperature range between 77 K and 900 K in β-$NaYF_4$. Another high-temperature limitation in this host is the phase transition to the cubic fluorite-type α polymorph, which occurs, however, at around 1050 K in the bulk compound and may be even at lower temperatures in nanocrystalline $NaYF_4$.[72]

Difference between microcrystalline and nanocrystalline samples and other practical problems

Another practical aspect is the usage of nanocrystalline core-only β-$NaYF_4$ instead of a microcrystalline powder. In that case, the surface-attached organic ligands or, alternatively, surrounding solvent molecules with X–H vibrational modes (X = C, N, O) dominate the nonradiative transitions within the Er^{3+} ion. While this fact accelerates the relaxation pathway from the green-emitting $^4S_{3/2}$ to the red-emitting $^4F_{9/2}$ level (one of the major reasons why core-only β-$NaYF_4$:Er^{3+},Yb^{3+} nanocrystals often show more dominant red upconverted emission upon NIR excitation),[62,73] the thermometrically relevant nonradiative $^2H_{11/2} \leftarrow {}^4S_{3/2}$ absorption transition is not significantly enhanced. As a consequence, the expected minimum onset temperature T_{on} for Boltzmann-type luminescence thermometry with Er^{3+} is generally higher in nanocrystalline β-$NaYF_4$ than in the analogous microcrystalline samples. Reported values for the average decay rate k_1 of the $^4S_{3/2}$ level of core-only β-$NaYF_4$:0.1 mol%Er^{3+} nanocrystals in various solvents are maximally $k_1 = 3$ ms^{-1} including the photonically induced enhancement due to the refractive index n of the solvent.[62] Assuming that there is a resonant vibrational mode that would allow a one-phonon bridging of the energy gap of $\Delta E_{21} = (650 \pm 10)$ cm^{-1}, it can be estimated from eqn (2) that the onset temperature could be even decreased to $T_{on} = 88$ K taking into account that the non-radiative coupling becomes stronger by around an order of magnitude to $k_{nr}(0) \approx 10$ μs^{-1} according to the energy gap law.[63]

In practice, however, higher activator fractions are used in nanocrystalline β-$NaYF_4$ for brighter upconversion emission upon NIR excitation. A competitive depopulation channel in such a case is cross-relaxation. It has been demonstrated that both at higher Er^{3+} and Yb^{3+} contents in β-$NaYF_4$, the $^4S_{3/2}$ level decays faster due to additional cross-relaxation based on an interaction with neighbouring Er^{3+} or Yb^{3+} ions. This is also the reason for the faster decay observed in the presented microcrystalline sample of β-$NaYF_4$:Er^{3+},Yb^{3+} (see Fig. 1(d)) and can be quantitatively assessed with the shell model of energy transfer.[62,74] In the following, I want to show that the choice of the right activator fractions is a compromise between the performance as a bright upconversion phosphor and the dynamic working range as a Boltzmann luminescent thermometer. Higher Er^{3+} and Yb^{3+} fractions and the consequent faster decay of the $^4S_{3/2}$ level (higher decay rate k_1) will lead to an increase of the expected onset temperature (see eqn (6)). Similar effects are known from *e.g.*, Nd^{3+}.[75,76] Therefore, it is generally recommended to use core–shell nanostructures and keep track of activator concentrations to limit internal cross-relaxation effects between Er^{3+} ions or between Er^{3+} and Yb^{3+} ions. For example, in core–shell nanocrystals of β-$NaYF_4$:2 mol%Er^{3+}, the average decay rate of the $^4S_{3/2}$ level increases to around $k_1 = 4$ ms^{-1},[62] while in the case of respective β-$NaYF_4$:2 mol%Er^{3+},18%Yb^{3+} nanocrystals, it even increases to $k_1 = 5$ ms^{-1}.[62] These values result in expected onset temperatures of $T_{on} = 106$ K and $T_{on} = 109$ K, respectively, still much below the optimum performance range according to eqn (2) assuming a similar non-radiative coupling rate as in microcrystalline samples. If, in addition, core-only nanocrystals are used, the respective decay rate increases to $k_1 = 8$ ms^{-1} (2 mol% Er^{3+}) and $k_1 = 10$ ms^{-1} (2 mol% Er^{3+}, 18 mol% Yb^{3+}),[62] resulting in maximum expected onset temperatures of $T_{on} = 115$ K and $T_{on} = 118$ K, respectively. Thus, although the additional quenching pathways in nanocrystalline upconversion phosphors can lead to a difference in the onset temperature of up to around 18 K, the effect is still not practically problematic if Er^{3+} is used as a Boltzmann thermometer in its optimum performance range at physiological temperatures (see eqn (2)). Yet, it is important to bear these effects in mind once lower temperatures are supposed to be measured with the green-emitting levels of Er^{3+} (although not thermodynamically recommendable). Overall, Er^{3+} is a particularly robust Boltzmann thermometer whose intrinsic electronic properties make it stand out compared to many other lanthanoid-based luminescent thermometers and support a unique, wide dynamic working range. The host compound β-$NaYF_4$ combines many beneficial features that make Er^{3+} perform almost at optimum theoretically suggested conditions both from a thermodynamic and kinetic perspective.

Conclusions

The upconversion phosphor β-$NaYF_4$:Er^{3+},Yb^{3+} is one of the working horse examples of a Boltzmann luminescent thermometer with a huge experimentally recorded success. In this tutorial work, it is demonstrated by recently developed thermodynamic and kinetic guidelines what makes Er^{3+} a primary candidate for Boltzmann thermometry. The green-emitting $^2H_{11/2}$ and $^4S_{3/2}$ levels of Er^{3+} are particularly suited for temperature measurements slightly above room temperature (between 275 K and 468 K) with highest possible statistical precision. The special feature of a higher spontaneous emission

rate of the higher energetic $^2H_{11/2}$ level in the Er^{3+} ion leads to a favourable electronic pre-factor C that ensures a LIR of the green emission bands close to 1 and is additionally beneficial for high readout precision. Besides those thermodynamic aspects, a unique property of Er^{3+} among the trivalent lanthanoid ions is the high non-radiative coupling strength between the $^2H_{11/2}$ and $^4S_{3/2}$ levels of $k_{nr}(0) = (2.29 \pm 0.54)\ \mu s^{-1}$, much stronger than for most other lanthanoid ions. This extraordinarily high value stems from an induced electric dipolar nature of the nonradiative transition and renders a particularly wide dynamic working range of Er^{3+} as a Boltzmann thermometer. It results in very low onset temperatures for thermal coupling of the green-emitting levels in the range of $T_{on} = (100 \pm 5)$ K. The host compound β-$NaYF_4$ with its low cutoff phonon energy of only 450 cm^{-1} is beneficial for a limitation of the nonradiative multiphonon relaxation of the $^4S_{3/2}$ level into the red-emitting $^4F_{9/2}$ level, even if already two phonon modes need to be consumed to bridge the energy gap of 650 cm^{-1} between the two green-emitting levels.

Two major competitive processes could potentially increase the onset temperature for Boltzmann behaviour of the LIR of the green emission bands of Er^{3+}. One of them is the previously indicated nonradiative relaxation pathway to the red-emitting $^4F_{9/2}$ level, which is more prominent in nanocrystalline (particularly core-only) β-$NaYF_4$:Er^{3+},Yb^{3+} due to the higher-energetic X–H (X = C, N, O) functional groups of surface-attached ligands or, alternatively, the surrounding solvent molecules. The other competitive pathway is cross-relaxation based on an interaction with neighbouring Er^{3+} and/or Yb^{3+} ions. Both described pathways effectively increase the total decay rate of the $^4S_{3/2}$ level and thus, the onset temperature T_{on}. It was demonstrated, however, that the respective onset temperatures for realistic values of typical activator concentrations in upconversion phosphors still remain below 120 K. Overall, Er^{3+} combines many of the theoretically suggested optimum conditions for a single-ion luminescent thermometer. Especially the strong intrinsic coupling between the two green-emitting $^2H_{11/2}$ and $^4S_{3/2}$ levels makes this ion particularly robust towards many disturbing excited state decay pathways and ensures that β-$NaYF_4$:Er^{3+},Yb^{3+} is one of the widest-range Boltzmann luminescent thermometers among all lanthanoid-activated inorganic compounds.

Data availability

Source data generated in this study, which are presented in the main text, are provided as a Source Data files *via* the Zenodo repository under accession code **https://doi.org/10.5281/zenodo.14738155**. Source data is also available from the corresponding author upon request.

Conflicts of interest

There are no conflicts to declare.

Acknowledgements

Financial support by a materials cost allowance of the Fonds der Chemischen Industrie e.V. and the "Young College" of the North-Rhine Westphalian Academy of Sciences, Humanities, and the Arts is gratefully acknowledged by the author.

References

1 S. W. Allison and G. T. Gillies, *Rev. Sci. Instrum.*, 1997, **68**, 2615–2650.
2 S. F. Collins, G. W. Baxter, S. A. Wade, T. Sun, K. T. V. Grattan, Z. Y. Zhang and A. W. Palmer, *J. Appl. Phys.*, 1998, **84**, 4649–4654.
3 P. R. N. Childs, J. R. Greenwood and C. A. Long, *Rev. Sci. Instrum.*, 2000, **71**, 2959–2978.
4 S. A. Wade, S. F. Collins and G. W. Baxter, *J. Appl. Phys.*, 2003, **94**, 4743–4756.
5 V. K. Rai, *Appl. Phys. B*, 2007, **88**, 297–303.
6 A. H. Khalid and K. Kontis, *Sensors*, 2008, **8**, 5673–5744.
7 C. D. S. Brites, S. Balabhadra and L. D. Carlos, *Adv. Opt. Mater.*, 2019, **7**, 1801239.
8 M. Suta and A. Meijerink, *Adv. Theory Simul.*, 2020, **3**, 2000176.
9 R. Marin, D. A. Gálico, R. Gayfullina, J. O. Moilanen, L. D. Carlos, D. Jaque and M. Murugesu, *J. Mater. Chem. C*, 2022, **10**, 13946–13953.
10 G. Brunet, R. Marin, M.-J. Monk, U. Resch-Genger, D. A. Gálico, F. A. Sigoli, E. A. Suturina, E. Hemmer and M. Murugesu, *Chem. Sci.*, 2019, **10**, 6799–6808.
11 S. Zanella, M. Aragon-Alberti, C. D. S. Brites, F. Salles, L. D. Carlos and J. Long, *Angew. Chem.*, 2023, **135**, e202306970.
12 M. D. Dramićanin, *J. Appl. Phys.*, 2020, **128**, 040902.
13 M. Suta, *Opt. Mater.: X*, 2022, **16**, 100195.
14 B. Bendel and M. Suta, *J. Mater. Chem. C*, 2022, **10**, 13805–13814.
15 C. D. S. Brites, K. Fiaczyk, J. F. C. B. Ramalho, M. Sójka, L. D. Carlos and E. Zych, *Adv. Opt. Mater.*, 2018, **6**, 1701318.
16 M. Sójka, J. F. C. B. Ramalho, C. D. S. Brites, K. Fiaczyk, L. D. Carlos and E. Zych, *Adv. Opt. Mater.*, 2019, **7**, 1901102.
17 M. Sójka, C. D. S. Brites and E. Zych, *J. Mater. Chem. C*, 2020, **8**, 10086–10097.
18 P. Bolek, J. Zeler, C. D. S. Brites, J. Trojan-Piegza, L. D. Carlos and E. Zych, *Chem. Eng. J.*, 2021, **421**, 129764.
19 M. Sójka, W. Piotrowski, L. Marciniak and E. Zych, *J. Alloys Compd.*, 2024, **970**, 172662.
20 T. Zheng, M. Sójka, M. Runowski, P. Woźny, S. Lis and E. Zych, *Adv. Opt. Mater.*, 2021, **9**, 2101507.
21 M. Sójka, M. Runowski, T. Zheng, A. Shyichuk, D. Kulesza, E. Zych and S. Lis, *J. Mater. Chem. C*, 2022, **10**, 1220–1227.
22 Z. Cao, X. Wei, L. Zhao, Y. Chen and M. Yin, *ACS Appl. Mater. Interfaces*, 2016, **8**, 34546–34551.
23 L. Cui, Z. Dong, D. Yu, Y. Wang and A. Meijerink, *Sci. Adv.*, 2024, **10**, eado7737.

24 J. C. Fister, D. Rank and J. M. Harris, *Anal. Chem.*, 1995, **67**, 4269–4275.
25 C. Baleizão, S. Nagl, S. M. Borisov, M. Schäferling, O. S. Wolfbeis and M. N. Berberan-Santos, *Chem. – Eur. J.*, 2007, **13**, 3643–3651.
26 A. Steinegger, I. Klimant and S. M. Borisov, *Adv. Opt. Mater.*, 2017, **5**, 1700372.
27 A. Steinegger and S. M. Borisov, *ACS Omega*, 2020, **5**, 7729–7737.
28 N. Menyuk, K. Dwight and J. W. Pierce, *Appl. Phys. Lett.*, 1972, **21**, 159–161.
29 K. W. Krämer, D. Biner, G. Frei, H. U. Güdel, M. P. Hehlen and S. R. Lüthi, *Chem. Mater.*, 2004, **16**, 1244–1251.
30 L. Wang and Y. Li, *Chem. Mater.*, 2007, **19**, 727–734.
31 F. Wang, Y. Han, C. S. Lim, Y. Lu, J. Wang, J. Xu, H. Chen, C. Zhang, M. Hong and X. Liu, *Nature*, 2010, **463**, 1061–1065.
32 H. Berthou and C. K. Jörgensen, *Opt. Lett.*, 1990, **15**, 1100–1102.
33 M. A. R. C. Alencar, G. S. Maciel, C. B. de Araújo and A. Patra, *Appl. Phys. Lett.*, 2004, **84**, 4753–4755.
34 F. Vetrone, R. Naccache, A. Zamarrón, A. J. de la Fuente, F. Sanz-Rodríguez, L. M. Maestro, E. M. Rodríguez, D. Jaque, J. G. Solé and J. A. Capobianco, *ACS Nano*, 2010, **4**, 3254–3258.
35 R. G. Geitenbeek, P. T. Prins, W. Albrecht, A. van Blaaderen, B. M. Weckhuysen and A. Meijerink, *J. Phys. Chem. C*, 2017, **121**, 3503–3510.
36 R. G. Geitenbeek, A. E. Nieuwelink, T. S. Jacobs, B. B. V. Salzmann, J. Goetze, A. Meijerink and B. M. Weckhuysen, *ACS Catal.*, 2018, **8**, 2397–2401.
37 T. Hartman, R. G. Geitenbeek, G. T. Whiting and B. M. Weckhuysen, *Nat. Catal.*, 2019, **2**, 986–996.
38 R. G. Geitenbeek, J. C. Vollenbroek, H. M. H. Weijgertze, C. B. M. Tregouet, A. E. Nieuwelink, C. L. Kennedy, B. M. Weckhuysen, D. Lohse, A. van Blaaderen, A. van den Berg, M. Odijk and A. Meijerink, *Lab Chip*, 2019, **19**, 1236–1246.
39 I. K. van Ravenhorst, R. G. Geitenbeek, M. J. van der Eerden, J. Tijn van Omme, H. H. Peréz Garza, F. Meirer, A. Meijerink and B. M. Weckhuysen, *ChemCatChem*, 2019, **11**, 5505–5512.
40 C. D. S. Brites, X. Xie, M. L. Debasu, X. Qin, R. Chen, W. Huang, J. Rocha, X. Liu and L. D. Carlos, *Nat. Nanotechnol.*, 2016, **11**, 851–856.
41 F. E. Maturi, R. S. R. Filho, C. D. S. Brites, J. Fan, R. He, B. Zhuang, X. Liu and L. D. Carlos, *J. Phys. Chem. Lett.*, 2024, **15**, 2606–2615.
42 T. P. van Swieten, T. Van Omme, D. J. Van Den Heuvel, S. J. W. Vonk, R. G. Spruit, F. Meirer, H. H. Pérez Garza, B. M. Weckhuysen, A. Meijerink, F. T. Rabouw and R. G. Geitenbeek, *ACS Appl. Nano Mater.*, 2021, **4**, 4208–4215.
43 Z. Ye, D. K. Bommidi and A. D. Pickel, *Adv. Opt. Mater.*, 2023, **11**, 2300824.
44 B. Harrington, Z. Ye, L. Signor and A. D. Pickel, *ACS Nanosci. Au*, 2023, **4**, 30–61.
45 A. R. N. Bastos, C. D. S. Brites, P. A. Rojas-Gutierrez, C. DeWolf, R. A. S. Ferreira, J. A. Capobianco and L. D. Carlos, *Adv. Funct. Mater.*, 2019, **29**, 1905474.
46 A. R. N. Bastos, C. D. S. Brites, P. A. Rojas-Gutierrez, R. A. S. Ferreira, R. L. Longo, C. DeWolf, J. A. Capobianco and L. D. Carlos, *Nanoscale*, 2020, **12**, 24169–24176.
47 X. Di, D. Wang, J. Zhou, L. Zhang, M. H. Stenzel, Q. P. Su and D. Jin, *Nano Lett.*, 2021, **21**, 1651–1658.
48 K. Wiwatowski, K. Sulowska, R. Houssaini, A. Pilch-Wróbel, A. Bednarkiewicz, A. Hartschuh, S. Maćkowski and D. Piątkowski, *Nanoscale*, 2023, **15**, 10614.
49 A. D. Pickel, A. Teitelboim, E. M. Chan, N. J. Borys, P. J. Schuck and C. Dames, *Nat. Commun.*, 2018, **9**, 4907.
50 A. D. Pickel and C. Dames, *J. Appl. Phys.*, 2020, **128**, 045103.
51 T. P. van Swieten, A. Meijerink and F. T. Rabouw, *ACS Photonics*, 2022, **9**, 1366–1374.
52 S. J. W. Vonk, T. P. van Swieten, A. Cocina and F. T. Rabouw, *Nano Lett.*, 2023, **23**, 6560–6566.
53 W. T. Carnall, H. Crosswhite and H. M. Crosswhite, *Technical Report: Energy level structure and transition probabilities in the spectra of the trivalent lanthanides in LaF_3*, Argonne National Lab, 1978 (report no.: ANL-78-XX-95). DOI: DOI: **10.2172/6417825**.
54 A. M. Kaczmarek, M. Suta, H. Rijckaert, A. Abalymov, I. Van Driessche, A. G. Skirtach, A. Meijerink and P. Van der Voort, *Adv. Funct. Mater.*, 2020, **30**, 2003101.
55 D. T. Klier and M. U. Kumke, *RSC Adv.*, 2015, **5**, 67149–67156.
56 G. Chen, H. Qiu, P. N. Prasad and X. Chen, *Chem. Rev.*, 2014, **114**, 5161–5214.
57 G. Yao, C. Link, Q. Meng, P. S. May and M. T. Berry, *J. Lumin.*, 2015, **160**, 276–281.
58 P. Villanueva-Delgado, D. Biner and K. W. Krämer, *J. Lumin.*, 2017, **189**, 84–90.
59 P. Rühl, D. Wang, F. Garwe, R. Müller, M. Haase, K. W. Krämer, W. Paa, R. Heintzmann, S. H. Heinemann and H. Stafast, *J. Lumin.*, 2021, **232**, 117860.
60 T. P. van Swieten, T. van Omme, D. J. van den Heuvel, S. J. W. Vonk, R. G. Spruit, F. Meirer, H. H. P. Garza, B. M. Weckhuysen, A. Meijerink, F. T. Rabouw and R. G. Geitenbeek, *ACS Appl. Nano Mater.*, 2021, **4**, 4208–4215.
61 R. G. Geitenbeek, H. W. de Wijn and A. Meijerink, *Phys. Rev. Appl.*, 2018, **10**, 064006.
62 F. T. Rabouw, P. T. Prins, P. Villanueva-Delgado, M. Castelijns, R. G. Geitenbeek and A. Meijerink, *ACS Nano*, 2018, **12**, 4812–4823.
63 L. A. Riseberg and H. W. Moos, *Phys. Rev.*, 1968, **174**, 429–438.
64 M. M. Lage, R. L. Moreira, F. M. Matinaga and J.-Y. Gesland, *Chem. Mater.*, 2005, **17**, 4523–4529.
65 B. R. Judd, *Phys. Rev.*, 1962, **127**, 750–761.
66 G. S. Ofelt, *J. Chem. Phys.*, 1962, **37**, 511–520.

67 T. P. van Swieten, J. M. Steenhoff, A. Vlasblom, R. de Berg, S. P. Mattern, F. T. Rabouw, M. Suta and A. Meijerink, *Light: Sci. Appl.*, 2022, **11**, 343.
68 M. J. Weber, *Phys. Rev.*, 1967, **157**, 262–272.
69 J. A. Capobianco, P. Kabro, F. S. Ermeneux, R. Moncorgé, M. Bettinelli and E. Cavalli, *Chem. Phys.*, 1997, **214**, 329–340.
70 C. Z. Bi, J. Y. Ma, J. Yan, X. Fang, D. Z. Yao, B. R. Zhao and X. G. Qiu, *Eur. Phys. J. B*, 2006, **51**, 167–171.
71 A. Sanson, M. Giarola, B. Rossi, G. Mariotto, E. Cazzanelli and A. Speghini, *Phys. Rev. B: Condens. Matter Mater. Phys.*, 2012, **86**, 21430.
72 O. Greis and J. M. Haschke, Chapter 45: Rare earth fluorides, in *Handbook on the Physics and Chemistry of Rare Earths*, ed. K. A. Gschneidner Jr. and L. Eyring, 1982, vol. 5, pp. 387–460.
73 M. J. J. Mangnus, V. R. M. Benning, B. Baumgartner, P. T. Prins, T. P. van Swieten, A. J. H. Dekker, A. van Blaaderen, B. M. Weckhuysen, A. Meijerink and F. T. Rabouw, *Nanoscale*, 2023, **15**, 16601–16611.
74 F. T. Rabouw, S. A. den Hartog, T. Senden and A. Meijerink, *Nat. Commun.*, 2014, **5**, 3610.
75 M. Suta, Ž. Antić, V. Đorđević, S. Kuzman, M. D. Dramićanin and A. Meijerink, *Nanomaterials*, 2020, **10**, 543.
76 A. Skripka, A. Benayas, C. D. S. Brites, I. R. Martín, L. D. Carlos and F. Vetrone, *Nano Lett.*, 2020, **20**, 7648–7654.